

# Motion Design for Grasp-Based Dynamic Locomotion in Microgravity

Chaerim Moon, Joohyung Kim, and Justin K. Yim

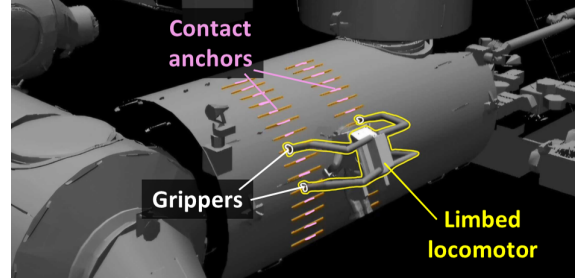
**Abstract**—Locomotion in microgravity often relies on sparsely and irregularly arranged anchors, motivating grasp-based mobility with multiple limbs. In this setting, dynamic locomotion is feasible only through deliberate regulation of both anchored interactions and whole-body coordination under coupled dynamic and kinematic constraints. This paper presents design insights for grasp-based dynamic locomotion with multi-limbed robotic systems in microgravity, targeting scenarios that require 6D limb manipulation to establish contacts with candidate anchors. The investigated design parameters include gait pattern, stride length, locomotion speed, and nominal posture. A parameterizable locomotion planning framework is proposed to support variations of these parameters and to evaluate the resulting locomotion performance in terms of stability and actuation demand. Two representative quadruped morphologies are adopted for evaluation in physics-based simulation. The results demonstrate that enlarging the feasible contact wrench space and attenuating impulsive whole-body dynamics improve locomotion performance. These findings inform strategies for contact configuration selection and whole-body coordination in microgravity locomotion with multi-limbed systems.

**Index Terms**—Legged Robots, Whole-Body Motion Planning, Multi-Limb Coordination, Contact Mechanics

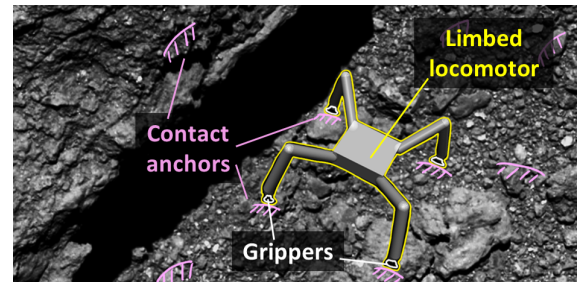
## I. INTRODUCTION

**L**OCOMOTION in microgravity is an essential capability in a broad range of space operations. For example, astronauts translate along existing handrails to inspect and maintain the exterior of the International Space Station (ISS) [1], [2]. Robonaut2, a humanoid robot, has been developed to assist such tasks, with the dexterity to operate structures and tools designed for humans [3]–[5]. Another application domain is space construction, where robots traverse sparse truss elements and assemble modular components to build in-orbit infrastructure [6]–[8]. Beyond these man-made environments, locomotion in natural settings, such as on the surfaces of asteroids for space mining [9], [10], offers additional opportunities and challenges for future space exploration.

Across both artificial and natural microgravity environments, feasible contact anchors are often sparsely distributed in 3D space, and in natural settings, they may be irregularly arranged. Such conditions inherently challenge locomotion strategies that rely on continuous ground contact, making limbed locomotors more viable than wheeled counterparts. However, microgravity introduces additional requirements compared to terrestrial locomotion, particularly in how a robot needs to regulate its interaction forces to achieve controlled



(a) Astronaut transport around the ISS



(b) Asteroid sample transfer

Fig. 1: Illustrative scenarios of grasp-based locomotion in low-gravity environments. (a) The ISS 3D models were obtained from [11], and (b) the background image of Ryugu is credited to JAXA, University of Aizu, and collaborators.

and reliable motion. Unlike terrestrial settings, where gravity-induced friction readily stabilizes motion, microgravity necessitates deliberate, anchored interactions. Consequently, grasp-based locomotion emerges as an effective and practical mode of mobility in these environments.

Despite its potential influence on space exploration, dynamic locomotion in microgravity remains insufficiently investigated. Many studies adopt quasi-static assumptions, treating inertial effects as negligible [12]–[14]. While effective for extremely cautious maneuvers, these approaches offer limited guidance for time-critical or energy-limited mission operations. Other efforts relax the quasi-static assumption and account for whole-body dynamics. Specifically, prior work suggests coordinating base and limb motions to restrain net momentum change to avoid detachment from contact surfaces [15]. However, this strategy still imposes unnecessary restrictions on the motion design space by restricting base translation to a separate phase after limb swinging. These limitations call for a systematic investigation into dynamic locomotion in microgravity.

This paper investigates locomotion design strategies for the distinct problem setting of microgravity, motivated by the scenarios illustrated in Fig. 1. The considered locomotion

The authors are with the Department of Mechanical Science and Engineering at the University of Illinois at Urbana-Champaign, USA. {cm74, joohyung, jkyim}@illinois.edu

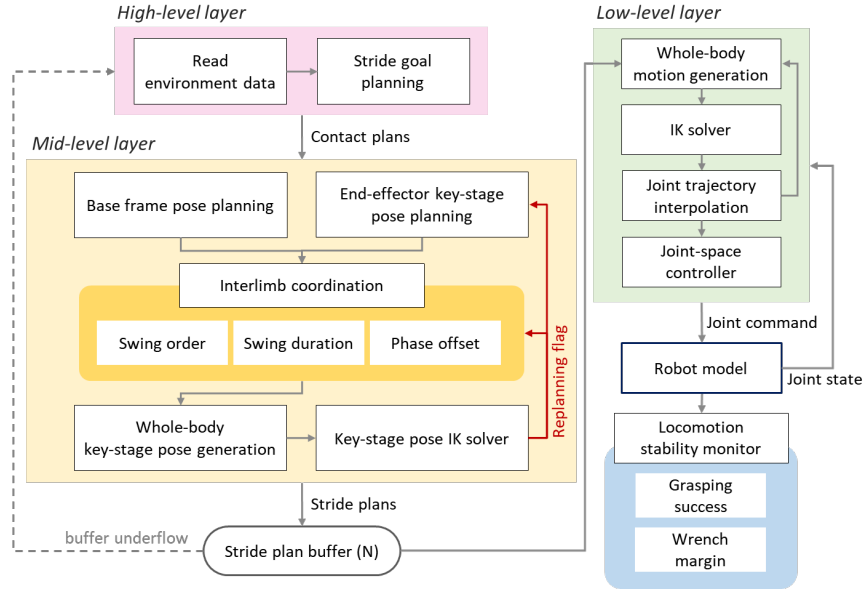


Fig. 2: Planning architecture for grasp-based microgravity locomotion with multi-limbed robotic systems. Each layer addresses distinct functions: stride goal planning; coordinated base and limb motion planning; and execution with real-time monitoring.

scenarios require full 6D limb manipulation to interact with the available contact anchors. The main contributions of this paper are summarized as follows:

- Formulation of dynamic and kinematic feasibility conditions for grasp-based dynamic locomotion in microgravity
- Development of a parameterizable locomotion planning architecture to support systematic exploration of gait parameters in multi-limbed robots
- Derivation of design insights relating contact and inertial constraints to locomotion performance (i.e., stability and actuation effort)

## II. RELATED WORK

Previous grasp-based locomotion studies provide useful insights into contact and whole-body motion requirements. Under Earth’s gravity, locomotion through grasping interactions with environmental structures (e.g., bouldering holds, poles, or walls) has been explored, especially in the context of climbing robots. In structured environments, traversal can be achieved by alternating hold-and-release sequences using grippers [16], [17]. Other approaches generate pushing forces against surrounding surfaces to exploit friction for support and propulsion [18], [19]. In both cases, reliable contact transitions are essential and often explored using sampling-based methods [13], [14], [20]; however, explicit consideration of whole-body dynamics remains limited. Related grasp-based locomotion concepts have also been studied in space robotics, mainly along two complementary directions. One is to regulate motion-induced inertial effects by designing swing motions that reduce momentum variation, along with base pose adjustment to compensate for the resulting whole-body momentum change [15], [21]. The other is to enlarge the admissible grasping range through gripper design, including electrostatic adhesion [22] and microspine-based anchoring [23].

Although previous studies have established important groundwork for grasp-based locomotion, including in low-

gravity settings, gaps remain in the investigation of generalizable feasibility conditions and the exploration of gait parameters.

## III. LOCOMOTION DESIGN CONSIDERATIONS

In the targeted scenario of grasp-based locomotion with full 6D limb manipulation, locomotion feasibility is governed by tightly coupled dynamic and kinematic considerations. This section defines the required fundamental feasibility constraints.

### A. Dynamic Feasibility

The criteria for assessing dynamic stability differ from those in terrestrial settings. In terrestrial locomotion, locomotion stability is often approximated using the support polygon [24]–[26]. In contrast, such simplifications no longer hold for grasp-based locomotion in microgravity, where key assumptions, including unilateral, compressive ground contact, are violated. Thus, a comprehensive analysis of the feasible 6D wrench space is required. It defines the range of whole-body accelerations that can be achieved without contact detachment, which is critical in microgravity, where contact loss may lead to uncontrolled drift and subsequent mission failure.

The feasible net contact wrench space can be represented as a wrench polytope, denoted as  $\mathcal{W}_{feasible} \subset \mathbb{R}^6$ , whose element is defined as  $\vec{W} = [\mathbf{f}^T \ \boldsymbol{\tau}^T]^T$ . It depends on parameters including grasp geometry, contact locations, allowable force directions and magnitudes, and friction constraints. The applied net wrench arises from various sources. Specifically,  $\vec{W}_{motion}$  denotes the wrench generated by the robot’s own motion-induced inertial effects, whereas  $\vec{W}_{others}$  captures additional wrenches arising from the unpredictable inertial effects associated with carried payloads or incidental collisions. Contact stability during locomotion requires this net wrench to remain within the feasible wrench space:

$$\vec{W}_{motion} + \vec{W}_{others} \in \mathcal{W}_{feasible} \quad (1)$$

This condition highlights two complementary ways to improve robustness. One is to enlarge the feasible wrench space  $\mathcal{W}_{feasible}$  through favorable contact configuration selection. The other is to limit the motion-induced wrench  $\vec{W}_{motion}$  through coordination of base and limb motions.

### B. Kinematic Feasibility

Grasp-based locomotion relies on consecutive anchor-to-anchor transitions, making kinematic feasibility an additional primary constraint. In 3D environments with sparsely placed feasible contact anchors, the system must reach and engage the scheduled anchors throughout the gait cycle. As a quadruped includes a floating base, base motion strongly affects this feasibility by shaping each limb’s attainable contact pose set in the world frame. It highlights the importance of regulating the relative geometry between the robot and its surrounding structures through base trajectory planning.

## IV. LOCOMOTION PLANNING FRAMEWORK

A motion planning framework is proposed for multi-limbed robotic systems operating in known, uneven 3D environments (Fig. 2). It supports systematic variation of robot morphology, gait pattern, stride length, locomotion speed, and nominal gait posture. Anchor identification and robot-to-anchor relative pose estimation are assumed to be provided by existing SLAM and vision-based perception modules; this work focuses on designing a computational architecture for coordinated whole-body planning.

### A. Motion Planning Architecture

The framework is organized into three layers: high-level, mid-level, and low-level planning. The high-level layer produces stride-wise discrete target poses. For each stride, the planner selects an initial subset of candidate contact anchors based on the prescribed stride length. Based on the selected anchor poses, the target base pose is adaptively calculated to enhance kinematic feasibility. The computed target base and end-effector poses are transmitted to the mid-level layer.

The mid-level layer realizes time-parameterized whole-body motion coordination. It begins by generating a base frame trajectory that connects the current and target base poses. In parallel, this layer defines end-effector paths for safe and predictable interactions with the anchors. Subsequently, base and limb motions are coordinated through interlimb parameters, including swing order and timing.

The low-level layer executes the coordinated motion by directly interfacing with the robotic system. Given motions from the mid-level layer, it solves the inverse kinematics to generate the corresponding joint commands. The resulting commands are then interpolated as necessary to satisfy the control rate of the hardware or simulation.

The framework operates with event-driven updates in the planning layers and fixed-rate execution at the controller interface (1 kHz). Planning is invoked on demand when a downstream module requests a successor stride plan, and the resulting trigger is propagated upstream across the hierarchy.

TABLE I: Swing Stages

Stage	Name	Description
$\sigma_1$	Release	Open the gripper; detach
$\sigma_2$	Normal Retreat	Retreat along contact normal
$\sigma_3$	Pure Transit	Translate toward the target
$\sigma_4$	Normal Approach	Approach along target normal
$\sigma_5$	Grasp	Close gripper; secure contact

### B. Base Frame Trajectory Planning

Desirable whole-body motion patterns differ between locomotion with and without gravity. In terrestrial and partial gravity locomotion, vertical oscillations of the center of mass (COM) are often exploited to capitalize on potential-kinetic energy exchange [27]–[29]. However, in microgravity, this mechanism is absent; vertical oscillations provide no energy benefit and instead introduce unnecessary momentum variations that increase grasping effort and the risk of contact loss. Accordingly, the base frame trajectory is designed to regulate variations in whole-body momentum while maintaining a prescribed clearance from the environment to avoid collisions.

For each stride, the target base frame pose, represented in 6D, is constructed from the upcoming set of contact points. The target base frame coordinate is defined using a best-fit plane of the target contact points: the plane normal defines the reference z-axis. The yaw is selected to align the base heading midway between the directions of the left and right limb sets. The in-plane (x-y) position of the base frame is set to the center of the contact points, while the z position is obtained by applying a fixed clearance offset from the plane, determined by the nominal gait posture.

The stride duration is computed to satisfy gait parameters, including base and swing speed and phase overlap constraints. Given this duration, the corresponding target base frame velocities are computed, and the base’s 6D trajectory is generated via a polynomial blended trapezoidal velocity profile to ensure  $C^2$  continuity to regulate momentum variations.

### C. End-Effector Trajectory Planning

The end-effector path is planned to enable each limb to interact with its target contact anchor safely and predictably, following the sequence summarized in Table I. In  $\sigma_2$  (Normal Retreat), the end-effector retreats along the current contact plane normal by a preset clearance margin, with the end-effector orientation aligned with the current contact frame to avoid collision between the gripper geometry and the interacting structure. In  $\sigma_3$  (Pure Transit), the end-effector executes the main transfer motion toward the target contact point whose trajectory can be expressed as  $T(t) = T_{naive}(t)T_{ref}(t)$ . It first sets a straight line interpolation from the current to the target contact point, which is denoted as  $T_{naive}(t)$ . Then, the reference transform  $T_{ref}(t)$  refines this motion, which defines interpolation from the current to the target contact pose applying a fixed clearance offset along the z-axis. In  $\sigma_4$  (Normal Approach), the end-effector approaches the target contact anchor along the target contact plane normal to initiate contact, with the orientation aligned with the target contact frame to avoid robot-environment collisions.

With stage motions defined, the end-effector swing trajectory is parameterized using quintic polynomial interpolation to ensure smooth motion. The boundary conditions enforce zero velocity and acceleration at the start of  $\sigma_2$  and the end of  $\sigma_4$ , mitigating impulsive effects at contact breakage and contact initiation. For stages through  $\sigma_2$  to  $\sigma_4$ , timings are allocated proportionally to each stage travel distance. The resulting phase schedule is later scaled by the swing duration determined downstream. The durations of the gripper operation stages  $\sigma_1$  &  $\sigma_5$  can be preset based on gripper actuation requirements (e.g., jaw closing, microspine engagement, etc.).

#### D. Interlimb-Parameterized Whole-Body Coordination

Given the base and end-effector trajectories, whole-body trajectory coordination is realized by interlimb parameters, including swing order, phase overlap, and swing duration. The swing order specifies the temporal sequence of limb swings within a stride and shapes the contact configurations. Phase overlap permits selected limbs to swing simultaneously, expanding the extent of achievable dynamic locomotion while reducing the average number of contact points. Addressing the calculated stride duration and overlap schedule, the swing duration per limb is allocated proportionally to its swing displacement.

#### E. Execution Support Modules

The locomotion plan modification module handles kinematic infeasibility not explicitly resolved by the global planner. It is triggered when the key-stage IK solver fails or when the resulting configuration is judged to be near a kinematic singularity. Here, key stages denote the full-body joint configurations at swing-phase boundaries. Depending on when the failure is detected, the module modifies swing order and/or refines the target contact pose using nearby reachable anchors while keeping the remaining gait parameters fixed. The process is repeated until a feasible solution is found or all candidate modifications are exhausted, in which case the trial is classified as a motion-planning failure.

A locomotion stability monitor is incorporated to detect grasp failures and incipient instability during gait execution. It evaluates grasp success using end-effector proximity and touch sensors, and assesses dynamic stability by comparing the estimated motion-induced whole-body wrench against the feasible contact wrench space. If either criterion indicates detachment risk or instability, the locomotion task is paused.

## V. SIMULATION

A physics-based simulation study is conducted in MuJoCo to investigate the correlation between parameters of interest and dynamic locomotion performance in the target scenario. All simulations are conducted under microgravity by configuring MuJoCo with zero gravitational acceleration (i.e.,  $\vec{g} = \vec{0}$ ).

#### A. Robot Models

For tractable evaluation, the framework is instantiated on a quadrupedal system, which represents a minimal morphology

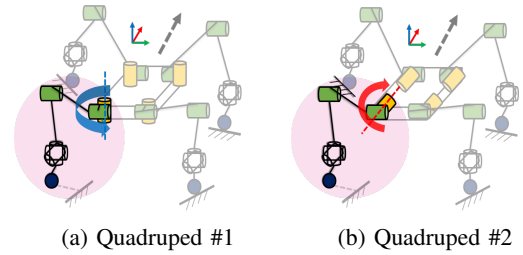


Fig. 3: Selected 6-DOF quadruped configurations. The distinction lies in the proximal chain: (a) YPP and (b) RPP.

that still supports nontrivial contact scheduling and transitions between support configurations with different numbers of active contacts. The robot consists of a rigid base and four identical 6-DOF limbs, each equipped with a gripper capable of generating pulling forces at the end-effector. Each limb comprises 2-DOF hip joints, a 1-DOF knee joint, and a 3-DOF ankle. The robot specifications are summarized in Table II. The base mass is chosen to dominate the limb masses to reflect heavy-load microgravity operation scenarios, and link masses are assigned in proportion to link lengths, assuming a uniform linear density of 1 kg/m.

Two quadruped morphologies are considered (Fig. 3): Yaw-Pitch-Pitch (YPP) [17], [30], [31] and Roll-Pitch-Pitch (RPP) [32]–[34], which differ in the proximal joint-axis configuration while sharing an identical distal chain. In both cases, the distal chain is configured as a spherical joint to align the end-effector orientation with the grasp pose.

Each limb is controlled using a position-based torque controller to track the planned motions while isolating the effects of gait parameters from controller-level optimization. Joint torques for both swing and stance are given by

$$\tau = M(q)(\ddot{q}_{des} + K_P e + K_D \dot{e}) + C(q, \dot{q}) \dot{q} \quad (2)$$

where  $M(q)$  denotes the joint-space inertia matrix,  $C(q, \dot{q})$  is the centrifugal and Coriolis term, and  $e = q_{des} - q$  and  $\dot{e} = \dot{q}_{des} - \dot{q}$  are the joint position and velocity tracking errors.  $K_P$  and  $K_D$  are the proportional and derivative gain matrices, respectively. Note that the gravity term is omitted due to the microgravity assumption.

In simulation, the end-effector geometry is abstracted as a sphere, and microspine grasping is abstracted as a bounded attachment interaction that captures load-limited engagement

TABLE II: Robotic System Specifications

Items	Specifications
base frame dimension	width: 0.60 m height: 0.70 m depth: 0.125 m
Link length	link 1: 0.676 m link 2: 0.806 m link 3: 0.200 m
Component mass	base frame: 200 kg joint 1,2,3: 2.93 kg joint 4,5,6: 0.48 kg
Joint torque limits	joint 1,2,3: 200 Nm joint 4,5,6: 19.94 Nm
Joint velocity limits	joint 1,2,3: 19.4 rad/s joint 4,5,6: 24.18 rad/s
max grasping force	260 N

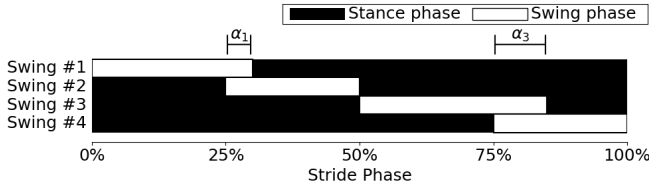


Fig. 4: Hildebrand diagram. Swing  $\#i$  is the  $i_{th}$  order of swinging limb in the stride. The temporal overlap between the  $i_{th}$  and  $(i+1)_{th}$  swings is denoted by  $\alpha_i$ .

and detachment. Attachment is implemented using MuJoCo’s adhesion actuator with explicit capacity limits, detaching when the load exceeds these limits. To improve contact stability, the gripper incorporates peripheral contact points that distribute attachment loads across multiple contacts, analogous to passive self-alignment in existing gripper designs. Grasping support is realized through modified friction coefficients. For contact wrench space evaluation, the contact model combines a polyhedral friction cone with a spherical, omnidirectional grasp model.

### B. Evaluation Scenarios

To investigate the gait parameters of interest, 100 randomized environments are generated for a 10 m forward traversal task. Each environment is constructed from 3D handrail pairs with sampled relative offsets and orientations to capture spatial irregularity and discreteness. Successive pairs are offset by  $[0.275, 0.325]$  m in  $x$ ,  $[-0.15, 0.15]$  m in  $y$ , and  $[-0.1, 0.1]$  m in  $z$ , and each handrail is independently rotated by up to 22.5 degrees about roll, pitch, and yaw. Within each pair, the  $y$ -separation is constrained to  $[1.6, 2.0]$  m, and the relative offsets in  $x$  and  $z$  are bounded within  $[-0.15, 0.15]$  m.

For each environment, a baseline gait and a set of parameter variants are simulated for two selected quadruped morphologies. The parameters considered are gait pattern, stride length, locomotion speed, and nominal posture, where gait pattern is characterized by swing order and swing phase overlap. In this study, the optimal swing order and phase overlap are defined as those that maximize support capability. Swing order optimality is evaluated using the contact configuration score:

$$s = w_a s_a + w_s s_s + w_b s_b, \quad s.t., \quad (3)$$

$$s_* := \min_{\mathbf{u}_* \in \mathcal{U}_*} \max_{\mathbf{f} \in \mathcal{W}_f} \left( \mathbf{f}^\top \mathbf{u}_{*,f} \right) \Delta x + \min_{\mathbf{u}_* \in \mathcal{U}_*} \max_{\boldsymbol{\tau} \in \mathcal{W}_\tau} \left( \boldsymbol{\tau}^\top \mathbf{u}_{*,\theta} \right) \Delta \theta \quad (3a)$$

where the scalars  $s_a$ ,  $s_s$ , and  $s_b$  are the support scores for arbitrary, swing-induced, and base motion-induced disturbances, respectively, and the nonnegative scalars  $w_a$ ,  $w_s$ , and  $w_b$  are the corresponding weighting coefficients. The vectors  $\mathbf{f} \in \mathbb{R}^3$  and  $\boldsymbol{\tau} \in \mathbb{R}^3$  denote the resultant support force and torque about the base frame, respectively, subject to friction and grasping-force constraints. The unit vector  $\mathbf{u}_{*,f} \in \mathbb{R}^3$  and  $\mathbf{u}_{*,\theta} \in \mathbb{R}^3$  denote the corresponding disturbance directions.  $\Delta x$  and  $\Delta \theta$  are the prescribed virtual linear and angular displacements used to combine the force and torque terms in a virtual-work-inspired manner. In each subscore, the minimization represents the score in the least resilient direction.

The optimal swing order maximizes the contact configuration score, while the optimal phase overlap is the minimum value satisfying the base translation, swing speed, and maximum allowable overlap constraints. This choice minimizes the duration of phases with a small number of supporting contacts, which would otherwise degrade support capability.

The baseline gait is defined by the opt swing order, a swing phase overlap of 30% of the shorter swing within each limb pair, a stride length of 0.6 m, a maximum base travel speed of 0.15 m/s, and a nominal base height of 0.8 m. Variants are generated by varying one parameter at a time while keeping the others at their baseline values. The tested variations are amble and trot for swing order, the optimal overlap and 50% overlap for swing phase overlap, 0.3 m for stride length, 0.10 m/s for maximum base travel speed, and 0.6 m for nominal base height.

These gait parameters characterize the gait cycle, along with a heuristic rule for phase overlaps among the limbs, as visualized in the Hildebrand diagram (Fig. 4). Overlap is permitted only for swing pairs (1-2) and (3-4) with the remaining swing transitions constrained to zero overlap to avoid prolonged two-limb support and the associated reduction in feasible wrench space. For each overlapping pair, the overlap is applied symmetrically and defined relative to the shorter swing duration.

For each parameter variant, comparison with the baseline is restricted to terrains on which both conditions successfully complete the 10 m traversal, yielding paired observations under identical terrain conditions. Statistical significance is assessed for each metric using a paired t-test at the 0.05 level. All trials use identical gripper limits and controller settings, and swing-order adjustment is disabled for the canonical swing order cases (i.e., amble and trot).

### C. Evaluation Metrics

Locomotion performance is quantified using metrics that capture support capability, motion-induced disturbances, and actuation effort, and all metrics are computed over the full trial interval. Support capability is evaluated using the contact configuration score (Eq. (3)), which reflects robustness to both unknown external disturbances and expected motion-induced disturbances. For each stride, distinct contact configurations determined by the designed gait cycle are identified, and their corresponding scores are computed. The final normalized score is then computed as the duration-weighted average of these configuration scores during their effective intervals.

Motion-induced disturbances are evaluated using two wrench-based metrics: whole-body motion-induced wrench and swing-induced wrench. For each metric, the peak and RMS values of force and torque magnitudes over the trial are used for comparison. The whole-body motion-induced wrench quantifies the net momentum variation induced by the planned gait motions under grasp support. At each timestep, the velocity of the robot COM is estimated, and its time derivative is used to calculate the whole-body motion-induced wrench. The resulting wrench signal is filtered using a moving-average window of 0.1 s. The swing-induced wrench quantifies

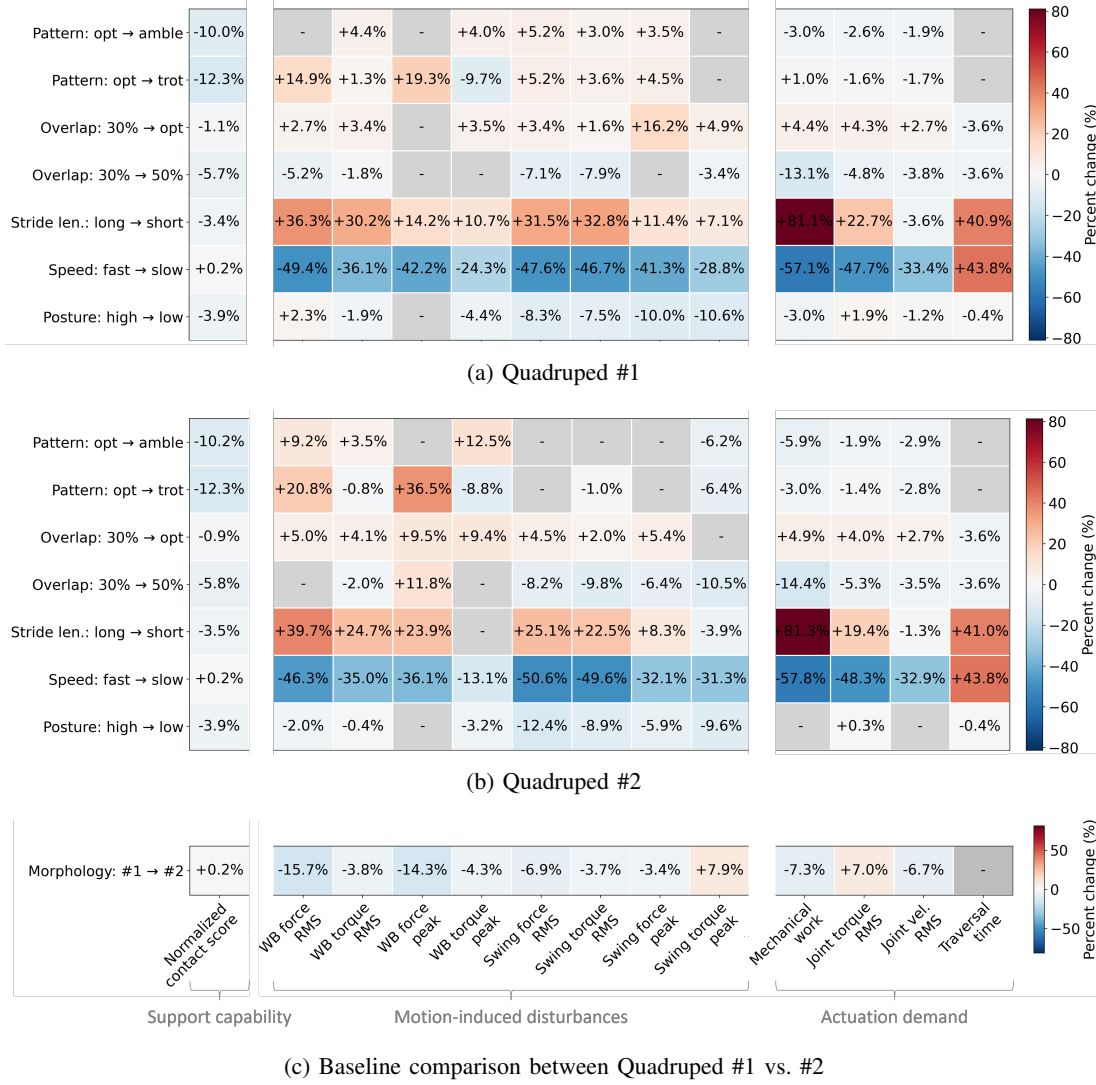


Fig. 5: Heatmaps of percentage changes in the performance metrics relative to the baseline gait for one-at-a-time parameter variants (a), (b) and morphology comparison (c). Grey area indicates no statistically significant difference ( $p > 0.05$ ).

the inertial wrench generated specifically by the swinging limbs; it measures the wrench transferred from the swinging limbs to the base frame, aggregated over all limbs in swing.

Actuation effort is captured by the total mechanical work:

$$W = \int_T \sum_j |\tau_j(t) \omega_j(t)| dt, \quad (4)$$

where  $\tau_j(t)$  and  $\omega_j(t)$  denote the actuating torque and angular velocity of joint  $j$ , respectively. Alongside total work, actuation demand is further characterized using the root-mean-square (RMS) joint torque and joint velocity over the trial interval. The elapsed time to complete the 10 m traversal, under fully accommodated gait parameter constraints, is reported as traversal time.

## VI. RESULTS

Over 100 randomized environments, the simulation studies evaluated the effects of gait pattern, phase overlap, stride length, base travel speed, and nominal posture on locomotion performance (i.e., stability and actuation effort) for two

TABLE III: Number of successful trials

variant	quadraped #1	quadraped #2
baseline	-	100
pattern	amble	86
	trot	76
overlap	opt	100
	50%	100
stride len.	short	100
speed	slow	100
posture	low	100
		99

\* Values indicate the number of successful 10m traversal trials out of 100 randomized environments for each condition.

quadraped morphologies. Successful trial counts for each condition are summarized in TABLE III, while performance changes relative to the baseline are summarized in Fig. 5.

### A. Swing Order and Phase Overlap Comparison

Swing order and phase overlap had the strongest influence on task success. The baseline optimized condition succeeded in all 100 trials for both morphologies, whereas canonical swing

orders reduced success rates by up to 26%. Most failures in amble were due to unavailable plans, while trot demonstrated relatively more failures due to limited feasible wrench space, a trend that became stronger at 50% overlap.

Across the two morphologies, the metric-level trends were broadly consistent. The opt swing order achieved the highest normalized contact score, followed by trot and amble. Amble produced comparatively modest changes, mainly increasing whole-body torque metrics, whereas trot increased whole-body force metrics while reducing peak torque. For overlap variations, the opt condition increased disturbance and actuation metrics while reducing traversal time, whereas the 50% overlap condition reduced contact score, swing-wrench metrics, and mechanical work, with shorter traversal times. These results indicate that optimized swing order and extended swing phase overlap improved the performance metrics of interest, although greater overlap degraded support capability.

### B. Stride Length and Speed Comparison

A shorter stride length produced the largest increases in disturbance, actuation, and traversal time for both morphologies. In contrast, slower base travel speed substantially reduced whole-body and swing-wrench metrics and mechanical work while leaving the normalized contact score nearly unchanged, although traversal time increased. These results suggest that longer stride lengths are generally favorable within kinematic limits, whereas slower speeds may be beneficial when traversal time is not a primary concern.

### C. Nominal Posture and Morphology Comparison

The posture variant produced the smallest overall changes. For both morphologies, the normalized contact score decreased, and swing wrench metrics were generally lower than in the baseline, while changes in whole-body wrench metrics, actuation demand, and traversal time remained minor. Comparing the baseline conditions, quadruped #2 generally showed lower disturbance- and effort-related metrics than quadruped #1. The majority of whole-body and swing-wrench metrics decreased, along with mechanical work, while swing peak torque and joint torque increased. These findings highlight that favorable nominal postures and robot morphologies can contribute to stable and efficient locomotion.

## VII. DISCUSSION

The simulation results suggest that microgravity locomotion performance is governed by the coupled effects of gait parameters. Task success was most strongly influenced by swing order flexibility, followed by support capability. This highlights the importance of adaptive swing sequencing in complex 3D environments while preserving support robustness.

For successful trials, variations in gait parameters revealed trade-offs among performance metrics. Support capability was governed by effective support geometry and contact redundancy. The normalized contact score increased under gait parameter settings with larger effective moment arms (e.g., optimized swing orders, longer stride lengths, and higher

nominal postures) and greater contact redundancy (e.g., lower swing phase overlap). However, support capability was not an isolated performance metric. Larger effective moment arms raised joint torque demand at stance limbs and sensitivity to disturbances, while greater contact redundancy increased traversal time. Support capability was also closely associated with whole-body motion-induced wrench. In the canonical swing order cases, lower support capability was accompanied by a larger whole-body motion-induced wrench, despite comparable swing-induced disturbance relative to the opt case, suggesting that better-conditioned support sets improve whole-body stability. Thus, parameters that improve support capability should be tuned with careful consideration of their combined effects on joint torques and traversal time.

Complementary trade-offs were also observed among motion-induced disturbance, actuation demand, and traversal time. Shorter swing phase overlap and slower base travel speed generally decreased motion-induced disturbance and actuation demand, but increased traversal time, suggesting that more dynamic locomotion is viable only when support capability is sufficiently well conditioned. By contrast, longer stride length also decreased motion-induced disturbance and actuation demand while shortening traversal time, indicating that longer stride lengths are generally preferable. However, stride length must not be so large as to induce kinematic infeasibility at the extremes of swing or stance. Nominal posture also influenced disturbance by altering the moment arm of swing-induced loading. In short, when tuning gait parameters to reduce motion-induced disturbance and actuation demand, the associated trade-offs in traversal time and kinematic feasibility need to be evaluated holistically.

The two morphologies exhibited similar qualitative relationships between gait parameters and performance metrics, with modest differences in magnitude. Quadruped #2 generally exhibited lower swing and whole-body motion-induced wrench metrics and lower mechanical work, likely due to kinematic characteristics that reduce the need for high joint velocities. However, this advantage came with higher joint torque, possibly reflecting a reduced ability to reject yaw-direction disturbances induced by limb swings. Thus, morphology selection should be guided by robot system specifications, as morphology shapes the trade-off between joint velocity and joint torque demands.

Overall, the observed trends indicate that microgravity locomotion is governed by the coupled effects of gait parameters. Across the tested conditions, favorable performance was associated with contact configurations that maintained robust support while limiting motion-induced wrench. Effective gait design for microgravity locomotion requires coordinated tuning of gait parameters to balance these two objectives.

This study uses a quadruped platform to investigate the parameters governing dynamic locomotion performance in microgravity. While the current validation is limited to quadrupeds, the framework is extendable to other limbed morphologies, such as bipeds and hexapods, with corresponding trade-offs in contact redundancy, dynamic feasibility, and kinematic complexity. The study also adopts simplifying assumptions, including prior environment knowledge and ab-

stracted grasping models, to isolate gait-parameter effects from perception and grasp uncertainty. Future work will relax these assumptions through SLAM-based environment estimation, probabilistic grasp-success modeling, and more sophisticated gripper-specific contact models.

## VIII. CONCLUSION

This study advances the understanding of grasp-based dynamic locomotion in microgravity, where robots interact with sparsely and irregularly distributed contact anchors while satisfying full 6D end-effector pose constraints. The results show that improved locomotion performance is most consistently achieved by selecting contact sets that enlarge the feasible contact wrench space and by coordinating limb motions to limit motion-induced wrenches. These findings provide a principled basis for designing robust and efficient grasp-based locomotion strategies in microgravity.

## REFERENCES

- [1] S. Korona, "Extravehicular activity development of unforeseen international space station maintenance." 46th International Conference on Environmental Systems, 2016.
- [2] S. K. Moore and M. A. Gast, "21st century extravehicular activities: Synergizing past and present training methods for future spacewalking success," *Acta Astronautica*, vol. 67, no. 7-8, pp. 739–752, 2010.
- [3] M. Diftler, T. Ahlstrom, R. Ambrose, N. Radford, C. Joyce, N. De La Pena, A. Parsons, and A. Noblitt, "Robonaut 2—initial activities on-board the iss," in *2012 IEEE Aerospace Conference*. IEEE, 2012, pp. 1–12.
- [4] M. A. Diftler, J. S. Mehling, M. E. Abdallah, N. A. Radford, L. B. Bridgwater, A. M. Sanders, R. S. Askew, D. M. Linn, J. D. Yamokoski, F. Permenter *et al.*, "Robonaut 2—the first humanoid robot in space," in *2011 IEEE international conference on robotics and automation*. IEEE, 2011, pp. 2178–2183.
- [5] F. Rehnmark, I. Spain, W. Bluethmann, M. Goza, R. O. Ambrose, and K. Alder, "An experimental investigation of robotic spacewalking," in *4th IEEE/RAS International Conference on Humanoid Robots, 2004.*, vol. 1. IEEE, 2004, pp. 366–384.
- [6] B. Jenett and K. Cheung, "Bill-e: Robotic platform for locomotion and manipulation of lightweight space structures," in *25th AIAA/AHS Adaptive Structures Conference*, 2017, p. 1876.
- [7] P. J. Staritz, S. Skaff, C. Urmson, and W. Whittaker, "Skyworker: a robot for assembly, inspection and maintenance of large scale orbital facilities," in *Proceedings 2001 ICRA. IEEE International Conference on Robotics and Automation (Cat. No. 01CH37164)*, vol. 4. IEEE, 2001, pp. 4180–4185.
- [8] P. Spino, D. Rus, F. Sebastianelli, O. Formoso, I. Kostitsyna, C. Gregg, and K. Cheung, "Proprioceptive inchworm robots for space applications," in *2025 IEEE Aerospace Conference*. IEEE, 2025, pp. 1–9.
- [9] K. Yoshida, T. Maruki, and H. Yano, "A novel strategy for asteroid exploration with a surface robot," *surgery*, vol. 5, p. 6, 2002.
- [10] A. Candalot, M.-M. Hashim, B. Hickey, M. Laine, M. Hunter-Scullion, and K. Yoshida, "Soft gripping system for space exploration legged robots," in *Climbing and Walking Robots Conference*. Springer, 2024, pp. 144–156.
- [11] NASA, "NASA 3D Resources - 3D Models," <https://github.com/nasa/NASA-3D-Resources/tree/master/3D%20Models>, 2024, accessed: 2025-06-14.
- [12] T. G. Chen, S. Newdick, J. Di, C. Bosio, N. Ongole, M. Lapôtre, M. Pavone, and M. R. Cutkosky, "Locomotion as manipulation with reachbot," *Science Robotics*, vol. 9, no. 89, p. eadi9762, 2024.
- [13] R. Zhang and J.-C. Latombe, "Capuchin: A free-climbing robot," *International Journal of Advanced Robotic Systems*, vol. 10, no. 4, p. 194, 2013.
- [14] T. Bretl, "Motion planning of multi-limbed robots subject to equilibrium constraints: The free-climbing robot problem," *The International Journal of Robotics Research*, vol. 25, no. 4, pp. 317–342, 2006.
- [15] W. F. Ribeiro, K. Uno, M. Imai, K. Murase, and K. Yoshida, "Ramp: Reaction-aware motion planning of multi-legged robots for locomotion in microgravity," in *2023 IEEE International Conference on Robotics and Automation (ICRA)*. IEEE, 2023, pp. 11 845–11 851.
- [16] Y. Tanaka, Y. Shirai, X. Lin, A. Schperberg, H. Kato, A. Swerdlow, N. Kumagai, and D. Hong, "Scaler: A tough versatile quadruped free-climber robot," in *2022 IEEE/RSJ International Conference on Intelligent Robots and Systems (IROS)*. IEEE, 2022, pp. 5632–5639.
- [17] K. Uno, N. Takada, T. Okawara, K. Haji, A. Candalot, W. F. Ribeiro, K. Nagaoka, and K. Yoshida, "Hubrobo: a lightweight multi-limbed climbing robot for exploration in challenging terrain," in *2020 IEEE-RAS 20th International Conference on Humanoid Robots (Humanoids)*. IEEE, 2021, pp. 209–215.
- [18] X. Lin, J. Zhang, J. Shen, G. Fernandez, and D. W. Hong, "Optimization based motion planning for multi-limbed vertical climbing robots," in *2019 IEEE/RSJ International Conference on Intelligent Robots and Systems (IROS)*. IEEE, 2019, pp. 1918–1925.
- [19] J. Zhang, X. Lin, and D. W. Hong, "Transition motion planning for multi-limbed vertical climbing robots using complementarity constraints," in *2021 IEEE International Conference on Robotics and Automation (ICRA)*. IEEE, 2021, pp. 2033–2039.
- [20] Z. Kingston and L. E. Kavraki, "Scaling multimodal planning: Using experience and informing discrete search," *IEEE Transactions on Robotics*, vol. 39, no. 1, pp. 128–146, 2022.
- [21] W. F. Ribeiro, K. Uno, M. Imai, K. Murase, B. C. Yalçın, M. El Hariry, M. A. Olivares-Mendez, and K. Yoshida, "Mobility strategy of multi-limbed climbing robots for asteroid exploration," in *Climbing and Walking Robots Conference*. Springer, 2023, pp. 33–45.
- [22] A. Xiang, L. Zhang, and L. Fan, "Design and analysis of an electro-adhesive hexapod robot with convertible limbs in microgravity," *Advances in Space Research*, vol. 73, no. 3, pp. 1908–1924, 2024.
- [23] A. Parness, "Anchoring foot mechanisms for sampling and mobility in microgravity," in *2011 IEEE International Conference on Robotics and Automation*. IEEE, 2011, pp. 6596–6599.
- [24] C. D. Bellicoso, F. Jenelten, P. Fankhauser, C. Gehring, J. Hwangbo, and M. Hutter, "Dynamic locomotion and whole-body control for quadrupedal robots," in *2017 IEEE/RSJ International Conference on Intelligent Robots and Systems (IROS)*. IEEE, 2017, pp. 3359–3365.
- [25] D. Pongas, M. Mistry, and S. Schaal, "A robust quadruped walking gait for traversing rough terrain," in *Proceedings 2007 IEEE International Conference on Robotics and Automation*. IEEE, 2007, pp. 1474–1479.
- [26] M. Kalakrishnan, J. Buchli, P. Pastor, M. Mistry, and S. Schaal, "Learning, planning, and control for quadruped locomotion over challenging terrain," *The International Journal of Robotics Research*, vol. 30, no. 2, pp. 236–258, 2011.
- [27] H. Geyer, A. Seyfarth, and R. Blickhan, "Compliant leg behaviour explains basic dynamics of walking and running," *Proceedings of the Royal Society B: Biological Sciences*, vol. 273, no. 1603, pp. 2861–2867, 2006.
- [28] M. Li, Z. Jiang, P. Wang, L. Sun, and S. S. Ge, "Control of a quadruped robot with bionic springy legs in trotting gait," *Journal of Bionic Engineering*, vol. 11, no. 2, pp. 188–198, 2014.
- [29] B. Han, H. Yi, Z. Xu, X. Yang, and X. Luo, "3d-slip model based dynamic stability strategy for legged robots with impact disturbance rejection," *Scientific Reports*, vol. 12, no. 1, p. 5892, 2022.
- [30] J. Hooks, M. S. Ahn, J. Yu, X. Zhang, T. Zhu, H. Chae, and D. Hong, "Alphred: A multi-modal operations quadruped robot for package delivery applications," *IEEE Robotics and Automation Letters*, vol. 5, no. 4, pp. 5409–5416, 2020.
- [31] S. Leuthard, T. Eugster, N. Faesch, R. Feingold, C. Flynn, M. Fritsche, N. Hürlimann, E. Morbach, F. Tischhauser, M. Müller *et al.*, "Magnecko: Design and control of a quadrupedal magnetic climbing robot," in *Climbing and walking robots conference*. Springer, 2024, pp. 55–67.
- [32] B. Katz, J. Di Carlo, and S. Kim, "Mini cheetah: A platform for pushing the limits of dynamic quadruped control," in *2019 international conference on robotics and automation (ICRA)*. IEEE, 2019, pp. 6295–6301.
- [33] M. Hutter, C. Gehring, D. Jud, A. Lauber, C. D. Bellicoso, V. Tsounis, J. Hwangbo, K. Bodie, P. Fankhauser, M. Bloesch *et al.*, "Anymal-a highly mobile and dynamic quadrupedal robot," in *2016 IEEE/RSJ international conference on intelligent robots and systems (IROS)*. IEEE, 2016, pp. 38–44.
- [34] M. Hutter, C. Gehring, M. Bloesch, M. A. Hoepflinger, C. D. Remy, and R. Siegwart, "Starleth: A compliant quadrupedal robot for fast, efficient, and versatile locomotion," in *Adaptive mobile robotics*. World Scientific, 2012, pp. 483–490.